Journal of Spacecraft and Rockets
Vol. 57, No. 5, September–October 2020

Removing Rate Unobservability in Sun-Heading Filters Without Rate Gyroscopes

Thibaud Teil,* Hanspeter Schaub,† and Scott Piggott‡
University of Colorado, Boulder, Boulder, Colorado 80303

https://doi.org/10.2514/1.A34704

In a sun-heading determination scenario, coarse sun sensors (CSSs) can be paired with rate gyroscopes in order to estimate sun-line direction and rotation rate. Relying solely on CSS measurements for sun-heading and spacecraft rotation rate estimations is advantageous in scenarios where reliance on the fewest number of devices is desired. Here, the challenge is to find a robust method for heading determination relying neither on rate gyroscopes nor on spacecraft dynamics. In such a scenario, the rotation rate of the spacecraft is estimated in order to provide state derivative control or simply for better sun-heading estimation. A novel sun-heading filter is derived that estimates only the observable components of the body-rate vector as the rate about the sun-heading axis remains unobservable. Elegantly switching between kinematic formulations to avoid singularities of one description, it provides not only better sun-heading estimates but also a partial body-rate estimate. The new filter is compared to two filters for gyroscopes-less sun-heading estimation. One comparison filter uses a projection method to remove the unobservable rate component, and another comparison filter uses numerical heading differences to estimate a rotation rate. The filters vary in state vectors, kinematics, and filter types, with the goal of controlling or removing nonobservability.

I. Introduction

Spacecraft pointing is an essential component to any mission scenario, whether it be to point a science instrument toward a target or a sun sensor toward the sun. Three-axis attitude estimation has been studied at length [1,2] with the use of a combination of many measurement types [3,4]. Although the star tracker provides a ubiquitous solution for inertial attitude pointing [5,6], many applications require relative pointing or secondary measurements to ensure the quality of the default instruments. This often leads to the problem of conducting reduced-attitude estimation [7], which can then be input to guidance and control schemes in order to point to (or away) from specific directions [8]. This paper develops a novel filter formulation in order to estimate a sun heading that is inertially fixed, using only coarse sun sensors (CSSs) as measurements, while also estimating the observable components of the body-rate vector.

CSSs are small, relatively inexpensive, and regularly used for sun-line heading determination. Cosine-type CSS devices output a voltage/current depending on the angle between the sensor normals and the sun direction. Although used in many micro- and nanosatellite missions [9,10], they are also widely used in cislunar missions including during safe mode [11]. More generally, heading determination provides target directions for the use of spacecraft pointing [11] or to solve for attitude [12]. As a two-degree-of-freedom measurement, one heading does not provide full attitude or rate information on its own. Previous work has efficiently used both rate gyroscopes and CSS measurements [13] for efficient sun-heading determination: notably during periods of eclipse. The gyroscopes help to forward integrate the sun-relative orientation until the spacecraft exits the eclipse. With enough CSSs (traditionally two pyramids of four with large fields of view), a spacecraft can always have at least one activated CSS, and frequently several activated devices. The resulting CSS data are sufficient for sun-heading determination during normal spacecraft operations. Outside of sun-heading estimation, gyroscopes are often used successfully for attitude and body-rate determination [14–16] while compensating for known or estimated drifts [17,18] and biases [19].

In contrast, some attitude determination modes use vector measurements [20] or quaternions [21] without gyroscopes. If the gyroscopes are not sufficiently accurate, as might be the case with low-cost microelectromechanical systems rate gyroscopes, this allows for a more robust sensor to determine attitude independently. Setting aside issues of observability, in a safe-mode scenario, it would also reduce the chances of using corrupted measurements (due to failed sensors) and would reduce the additional sensors' associated power draw. Spacecraft dynamics properties have been used to observe the full rate vector [22] through gyroscopic coupling. Yet, not using such dynamics also allows for minimalist and robust estimation. Mass properties change during the mission, particularly between trajectory correction maneuvers or insertion maneuvers. By being agnostic to mass properties and current actuator use, one filter can provide sun-heading information throughout a mission. In a safe-mode context, the desire remains to use as little information as possible. If any actuators malfunction and their properties are hard coded in the filter, its state estimation will be compromised because the filter dynamics will be incorrect.

Given these two challenges, this paper develops a novel kinematic formulation for sun-heading estimation. This formulation decouples the unobservable rate from the state vector. In previous works [23,24], the spacecraft body rate relative to the inertial frame is not estimated by the filter. To do this, a frame switching paradigm is implemented in order to avoid singularities, similarly to how modified Rodrigues parameters (MRPs) switch between alternate representations [25]. This implies rotating the states and covariance matrix when singularities are approached, tracking the frames of interest, as well as deriving a mapping of the state noise compensation on the covariance.

After illustrating the observability problems at hand, this paper derives five filters and compares their performances. The first filter only estimates the sun-heading vector, and it computes a partial solution to the satellite rotation rate at every step using the sun-heading estimates. The second and third subtract the unobservable components out of the states in an extended Kalman filter (EKF) and a square-root unscented Kalman filter (SR-UKF), respectively. In the final formulation, the kinematics of the problem are reduced to a five-by-one vector estimating the sun direction and the observable rotation rate by tracking two different frames. This yields a minimal state

---

Presented at the 29th AAS/AIAA Space Flight Mechanics Meeting, Maui, HI, January 13–17, 2019; received 12 November 2019; revision received 21 February 2020; accepted for publication 1 March 2020; published online 22 April 2020.

*Graduate Research Assistant, 431 UCB, Colorado Center for Astrodynamics Research, Department of Aerospace Engineering Sciences. Member AIAA.

†Glenn L. Murphy Chair of Engineering, Department of Aerospace Engineering Sciences. Fellow AIAA.

‡ADCS Integrated Simulation Software Lead, 1234 Innovation Drive, Laboratory for Atmospheric and Space Physics.

vector with no unobservable states and is the main contribution. By switching between two frames, the singularities can be avoided. As a novel derivation, it presents a promising approach to decoupling one of the observability problems in heading filters. This formulation is implemented in an EKF and a SR-UKF, and they are referred to as switch filters.

II. Problem Statement and Notations

A. Scenario Description

This study analytically develops five filters, of which two are new sequential sun-heading and rate estimators, and compares their performance to the three other gyroscopes-less filter implementations. To compare the filters, a scenario is created where a spacecraft is tumbling in deep space, and it attempts to determine its sun-heading direction and rotation rate vector. A simplified version of this scenario is pictured in Fig. 1 to illustrate a sensor normal and sun heading for a spacecraft.

The sun-heading vector is estimated as a nonunit vector due to scale factors from the instruments [26]. Indeed, $\boldsymbol{d} = C\hat{\boldsymbol{d}}$, where C is an instrument scale factor determined during ground testing using a calibration flux. It is not desired to estimate C in this work; therefore, $\boldsymbol{d}$ is estimated directly. The sun-heading vector in the body frame is written ${}^{\mathcal{B}}\boldsymbol{d}$, its inertial derivative is $\dot{\boldsymbol{d}}$, and its body frame derivative is $\boldsymbol{d}'$. The direction cosine matrix from an arbitrary $\mathcal{S}$ frame into the spacecraft body frame $\mathcal{B}$ will be $[\mathcal{BS}]$, and the inertial frame is labeled $\mathcal{N}$. Finally, the rotation rate between two frames is noted $\omega_{\mathcal{BN}}$, and the $[\tilde{\boldsymbol{\omega}}]$ represents the skew-symmetric matrix such that, for any $\boldsymbol{a} \in \mathbb{R}^3$, $[\tilde{\boldsymbol{\omega}}]\boldsymbol{a} = \boldsymbol{\omega} \times \boldsymbol{a}$. The filtering notation used complies with chapter 4 of Ref. [27], and the dynamics notation complies with Ref. [28].

The simulations are run with inputs listed in Table 1, where $\boldsymbol{\sigma}_{\mathcal{BN}}$ is the attitude of the body frame $\mathcal{B}$ with respect to the inertial frame $\mathcal{N}$ expressed as a modified Rodrigues parameter, $\boldsymbol{\omega}_{\mathcal{BN}}$ is the body rotation rate with respect to the inertial frame, and $[I]$ is the spacecraft inertia. This framework allows for a fully coupled dynamic simulation, and the runs use the same physical scenario (including noise), with only the filters changing between runs. The rates chosen are typical of spacecraft tipoff rates postseparation; this is seen on page 25 of the NanoRacks interface document,[§] where CubeSats are expected to be able to control up to 3 deg/s upon separation.

B. Measurements

The measurement model for CSSs has been studied previously in the literature: notably in Ref. [29], which provided a compact measurement model by assuming each CSS has a counterpart with opposite normal. Opposing sensors are also used in this work but using a slightly different notation:

$$G_i(\boldsymbol{X}) = \hat{\boldsymbol{n}}_i \cdot \boldsymbol{d} + \epsilon_i \tag{1}$$

where ϵ_i are components of the measurement noise vector modeled by a Gaussian distribution $\mathcal{N}(0, 0.018)$. The intensity of the signal is included in the $\boldsymbol{d}$ term as stated in the previous subsection. A standard deviation of 0.017 radiants corresponds to errors of ±2 deg on each measurement, which is a conservative distribution, given the values published by Adcole Aerospace.[¶]

The linearized measurement model $[H]$ is defined as $[H] = [\partial \boldsymbol{G}(\boldsymbol{X})/\partial \boldsymbol{X}]^*$, where $\boldsymbol{X}$ is the corresponding filter state vector, the right superscript star signifies that the partial is evaluated at the reference state, and $\boldsymbol{G}$ is the measurement model. In the following filters, the only measurements used are from the N CSS devices. For the ith sensor, the measurement is simply given by the dot product of the sun-line heading and the normal to the sensor, which defines each of the components of $\boldsymbol{G}$.

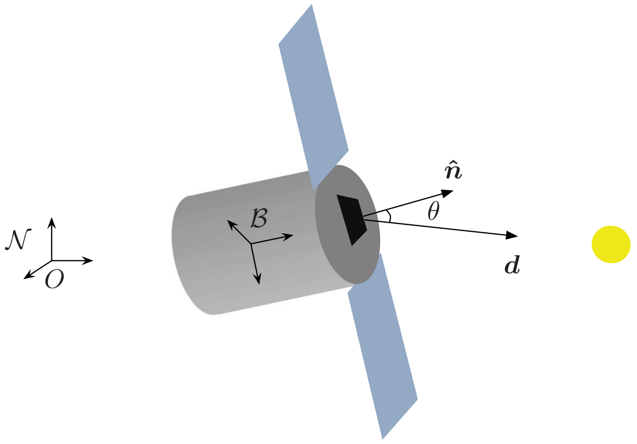

Fig. 1 Spacecraft equipped with a CSS.

In this application, the normals are listed in Table 2. This yields the partial derivatives for the $[H]$ matrix:

$$[H] = \begin{bmatrix} {}^{\mathcal{B}}\hat{\boldsymbol{n}}_1^T & [0_{1\times(n-3)}] \\ \vdots & \vdots \\ {}^{\mathcal{B}}\hat{\boldsymbol{n}}_N^T & [0_{1\times(n-3)}] \end{bmatrix} \tag{2}$$

where the rows contain the transposed normal vectors of the sensors that received measurements. The left-exponent notation indicates the frame with respect to which the vector components are taken. Hence, the $[H]$ matrix has a changing size depending on the amount of measurements. Additionally, the size of the $[H]$ matrix depends on the number of states n, as seen in Eq. (2).

The term "field of view" is used to describe the half-angle to the cone of visibility for each individual sensor. CSSs can have a variety of different specifications, depending on the instrument quality and its intended use. Adcole Aerospace displays a variety of different sensors with field-of-view angles between 30 and 85 deg. CSSs can come in preconstructed pyramids in order to get 2π steradian coverage, or individually such that they can be set at optimal locations on the spacecraft. A common practice (demonstrated, for instance, by the microwave anisotropy probe [29,30]) is to set the instruments on the tip of the solar panels in order to avoid any self-reflectance or self-shadowing.

Throughout this paper, a double pyramid of four CSS devices each is used. The normals for each of the sensors are displayed in Table 2 and allow for maximal sensor coverage. The field of view of each of these sensors will dictate the number of sensors that are activated for a specific attitude.

C. Observability

In the absence of rate gyroscopes, it is preferable to estimate the spacecraft rate, both for better states estimation and eventually for control. However, the desire to use CSS-only measurements for sun-heading determination exposes two observability issues. The first issue is that the spacecraft rotation vector's component about the sun-heading direction is unobservable. To use it more reliably in safe

Table 1 Simulation parameters

Parameter	Value
$\boldsymbol{\sigma}_{\mathcal{BN}}(t_0)$	$[0, 0, 0]^T$
$\boldsymbol{\omega}_{\mathcal{BN}}(t_0)$, deg/s	$[0.5, -0.5, -1]^T$
$[I]$, kg/m^2	diag(900, 800, 600)
Mass, kg	750
Simulation time, s	500

[§] Data available online at http://nanoracks.com/wp-content/uploads/NanoRacks-CubeSat-Deployer-NRCSD-Interface-Definition-Document.pdf [retrieved 01 March 2020].

[¶] Data available online at https://www.adcole.com/aerospace/analog-sun-sensors/coarse-sun-sensor-pyramid [retrieved 01 March 2020].

Table 2 CSS constellation

CSS group	${}^{\mathcal{B}}\hat{\boldsymbol{n}}_1$	${}^{\mathcal{B}}\hat{\boldsymbol{n}}_2$	${}^{\mathcal{B}}\hat{\boldsymbol{n}}_3$	${}^{\mathcal{B}}\hat{\boldsymbol{n}}_4$
1	$\left[\frac{\sqrt{2}}{2}, -0.5, 0.5\right]^T$	$\left[\frac{\sqrt{2}}{2}, -0.5, -0.5\right]^T$	$\left[\frac{\sqrt{2}}{2}, 0.5, 0.5\right]^T$	$\left[\frac{\sqrt{2}}{2}, 0.5, 0.5\right]^T$
2	$\left[-\frac{\sqrt{2}}{2}, -0.5, 0.5\right]^T$	$\left[-\frac{\sqrt{2}}{2}, -0.5, -0.5\right]^T$	$\left[-\frac{\sqrt{2}}{2}, 0.5, -0.5\right]^T$	$\left[-\frac{\sqrt{2}}{2}, 0.5, 0.5\right]^T$

mode, there needs to be progress made on this front: notably, by decoupling the unobservable component from the states and eventually observing it through novel methods. Caution must be exercised regarding limited rate estimation using such measurements. Lessons learned from the Lewis spacecraft [31,32] show that unobservable rate components can build up without the attitude determination algorithm realizing it. If it is desirable to do full rate estimation using CSSs only, the dynamics must be added to couple the unobservable rate through Euler's equation [24]. This does require the use of potentially changing dynamics in the filter, which is undesirable for a minimalist and robust formulation. The second challenge is due to the fact that, depending on the CSS field of view, the problem can suffer from a more general lack of observability. The field of view designates the cone in which each individual sensor can be activated by incoming sunlight. This unobservability is due to the nature of CSS measurements [33] because they only provide angular information between the sensor normal and the sun heading. This means that one CSS yields a cone of possibilities for the sun direction, two sensors lead to two possibilities, and only with three or more activated sensors do you get full observability instantaneously. If the sensors have a limited field of view, the spacecraft can go through time spans with little information: not enough to determine the sun heading uniquely.

The term field of view is used to describe the half-angle to the cone of visibility for each individual sensor. The analysis in this paper will focus on two values for the field of view of 85 and 60 deg, which will lead to a different number of active sensors at a given time. Figure 2 shows the number of activated CSSs for all longitudes and attitudes of the sun vector in the spacecraft body frame. The red dots correspond to the CSS normal directions, and the lighter colors represent areas of the 4π-steradian sphere with more overlapping CSS visibility cones. Figure 2a shows the relative sparsity in measurements with a narrow field of view per instrument head: there are large areas with only one or two active sensors. Figure 2b, on the other hand, shows that, with a wider field of view, there can be majority of four active sensors.

It is key to remember that this observability issue occurs in addition to the rate component being unobservable. There are therefore two issues: the sparsity of measurements at times that leads to a partially observable state, and a physically unobservable rate component along the sun-heading direction. Figures 2a and 2b only speak to the former. The latter is the object of the kinematics derived in this work.

III. Filter Kinematics

There are many possible implementations of gyroscopes-less sun-heading filters [34]. This subsection describes the formulations of previously implemented filters. This development sets up the mathematical frame work of CSS filters and illustrates the particular challenges of these solutions. The EKF algorithm used in these

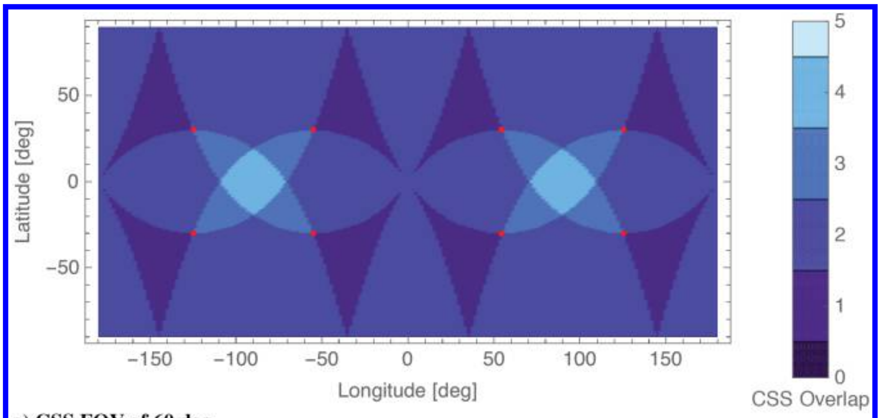

a) CSS FOV of 60 deg

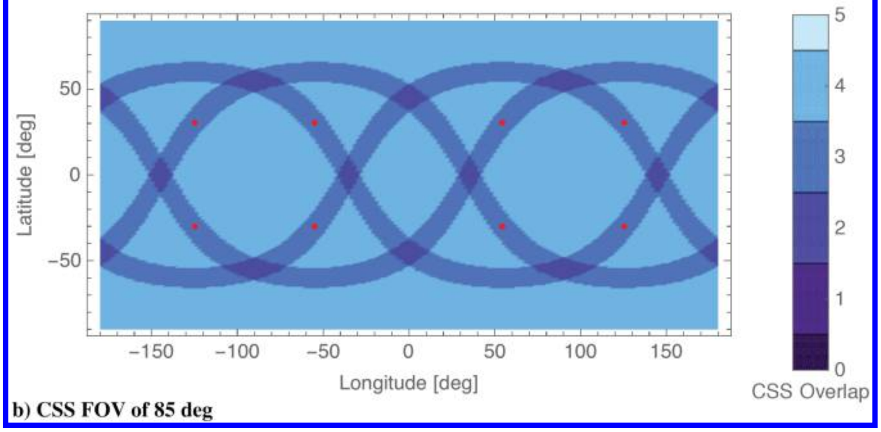

b) CSS FOV of 85 deg

Fig. 2 CSS coverage map illustrations. CSS headings are shown as red dots.

developments is explained and derived from Ref. [27]. All the filters have added process noise sampled from a Gaussian distribution.

A. Sun-Heading EKF

The sun-heading EKF ("sun-EKF" in following numerical simulations) is developed to use rate gyroscopes measurements if they are available. In the case in which they are not, the rate is computed with the two previous sun-heading estimates. The state vector of this filter only contains the sun-line vector in body frame components: $\boldsymbol{X} = {}^{\mathcal{B}}\boldsymbol{d}$. Given the nature of the filter, there is no unobservable rate component because the body frame derivative of $\boldsymbol{d}$ is not estimated. Despite this, there can still be poor observability of the heading direction if few sensors are activated. This solution is very simple, yet it has been shown to provide suitable sun-pointing performance in a safe-mode scenario [33]. This filter is included in the performance comparison because it provides an interesting benchmark to compare the more sophisticated filters again.

The propagation function $\boldsymbol{F}$ is

$$\boldsymbol{X}' = \boldsymbol{F}(\boldsymbol{X}) = {}^{\mathcal{B}}\boldsymbol{d}' = -[\tilde{\boldsymbol{\omega}}_{\mathcal{B}\mathcal{N}}]{}^{\mathcal{B}}\boldsymbol{d} \tag{3}$$

$${}^{\mathcal{B}}\boldsymbol{d}_{k+1} = {}^{\mathcal{B}}\boldsymbol{d}_k - \Delta t[\tilde{\boldsymbol{\omega}}_{\mathcal{B}\mathcal{N}}]{}^{\mathcal{B}}\boldsymbol{d}_k \tag{4}$$

and is discretized using an Euler integration in Eq. (4) with k indicating an indice representing discrete times in the estimation process. This provides a simple and fast integration scheme. As a reminder, the tilde operator in Eq. (3) is the matrix representation of the cross operator.

Next the state dynamics matrix $[A]$ is found through

$$[A] = \left[\frac{\partial \boldsymbol{F}(\boldsymbol{d}, t_i)}{\partial \boldsymbol{d}}\right] = -\left[\,\tilde{\boldsymbol{\omega}}_{\mathcal{B}\mathcal{N}}\,\right] \tag{5}$$

Gyroscopes measurements are not being read by the filter but can be approximated [23,24] by logging an extra time step of the sun-heading vector estimate $\boldsymbol{d}$:

$$\boldsymbol{\omega}_k = \frac{1}{\Delta t}\frac{\boldsymbol{d}_k \times \boldsymbol{d}_{k-1}}{\|\boldsymbol{d}_k \times \boldsymbol{d}_{k-1}\|}\arccos\left(\frac{\boldsymbol{d}_k \cdot \boldsymbol{d}_{k-1}}{\|\boldsymbol{d}_k\|\|\boldsymbol{d}_{k-1}\|}\right) \tag{6}$$

Equation (6) uses the shorthand notation $\boldsymbol{\omega}$ to signify $\boldsymbol{\omega}_{\mathcal{B}\mathcal{N}}$. Aliasing or noise issues are inherent to such a formulation. If the measurement times are too far apart with regard to the rate of change of the system, the rate may be poorly represented. On the other hand, if measurements are very close in time, the two vectors that are being crossed are nearly colinear. This will lead to noise being amplified and an incorrect estimate of $\boldsymbol{\omega}$. This method is not expected to produce good estimates for rate; yet, it has still been used successfully for attitude control in the literature [23]. It is therefore presented as a method of comparison. Given a noise distribution on the state $\boldsymbol{d}_k$ terms (characterized by the covariance), the uncertainty over the $\boldsymbol{\omega}_k$ term can be derived in order to quantify the error amplification. Although this would better describe this method and its pitfalls, it is not the goal of this work.

B. Subtracting Unobservability

The second filter derivation (called "EKF" and "SR-UKF" in the following numerical simulations) solves the rate unobservability by subtracting, from the state, the rate component along the sun-heading axis. The states that are estimated in this filter are the sun-line vector and its rate of change in the body frame $\boldsymbol{X} = [{}^{\mathcal{B}}\boldsymbol{d} \quad {}^{\mathcal{B}}\boldsymbol{d}']^T$.

The dynamics are given in

$$\boldsymbol{X}' = \boldsymbol{F}(\boldsymbol{X}) = \begin{bmatrix} \boldsymbol{F}_1(\boldsymbol{d}) \\ \boldsymbol{F}_2(\boldsymbol{d}') \end{bmatrix} = \begin{bmatrix} \boldsymbol{d}' - (\boldsymbol{d}\cdot\boldsymbol{d}')\dfrac{\boldsymbol{d}}{\|\boldsymbol{d}\|^2} \\ -\frac{1}{\Delta t}(\boldsymbol{d}\cdot\boldsymbol{d}')\dfrac{\boldsymbol{d}}{\|\boldsymbol{d}\|^2} \end{bmatrix} \tag{7}$$

The $\boldsymbol{F}_2(\boldsymbol{d}') = \boldsymbol{d}''$ function is identified via $\boldsymbol{F}_1$. Indeed, the subtraction of the unobservable components does not stem from spacecraft dynamics, yet it must be accounted for in the propagation. Therefore, the integration step (forward Euler) is used to compute the $\boldsymbol{F}_2$ function that propagates the rates:

$$\boldsymbol{d}'_{k+1} = \boldsymbol{d}'_k - (\boldsymbol{d}\cdot\boldsymbol{d}')\frac{\boldsymbol{d}}{\|\boldsymbol{d}\|^2} \tag{8}$$

$$\Rightarrow \frac{\boldsymbol{d}'_{k+1} - \boldsymbol{d}'_k}{\Delta t} = -\frac{1}{\Delta t}(\boldsymbol{d}\cdot\boldsymbol{d}')\frac{\boldsymbol{d}}{\|\boldsymbol{d}\|^2} \tag{9}$$

$$\Rightarrow \boldsymbol{d}''_{k+1} = -\frac{1}{\Delta t}(\boldsymbol{d}\cdot\boldsymbol{d}')\frac{\boldsymbol{d}}{\|\boldsymbol{d}\|^2} \tag{10}$$

Given the nature of the filter, the rotation about the $\boldsymbol{d}$ axis remains unobservable. To remedy this, the states are projected along this axis and subtracted in order to measure only observable state components. This is seen in the subtraction of $(\boldsymbol{d}\cdot\boldsymbol{d}')\cdot\boldsymbol{d}$ after normalization in both heading and heading-rate terms. Equation (10) shows the dependency on the integration time step in order to remove the unobservable components during the propagation. This displays one of the weaknesses of this method, and it provides another reason to improve upon the sun-heading determination method.

Using $[I]$ as a standard notation for the identity matrix, the associated state dynamics matrix $[A]$ is found through

$$[A] = \begin{bmatrix} \dfrac{\partial \boldsymbol{F}_1(\boldsymbol{X}, t_i)}{\partial \boldsymbol{d}} & \dfrac{\partial \boldsymbol{F}_1(\boldsymbol{X}, t_i)}{\partial \boldsymbol{d}'} \\ \dfrac{\partial \boldsymbol{F}_2(\boldsymbol{X}, t_i)}{\partial \boldsymbol{d}} & \dfrac{\partial \boldsymbol{F}_2(\boldsymbol{X}, t_i)}{\partial \boldsymbol{d}'} \end{bmatrix}$$
$$= \begin{bmatrix} -\left(\dfrac{\boldsymbol{d}'\boldsymbol{d}^T}{\|\boldsymbol{d}\|^2} + (\boldsymbol{d}\cdot\boldsymbol{d}')\dfrac{\|\boldsymbol{d}\|^2[I] - 2\boldsymbol{d}\boldsymbol{d}^T}{\|\boldsymbol{d}\|^4}\right) & [I] - \dfrac{\boldsymbol{d}\boldsymbol{d}^T}{\|\boldsymbol{d}\|^2} \\ -\dfrac{1}{\Delta t}\left(\dfrac{\boldsymbol{d}'\boldsymbol{d}^T}{\|\boldsymbol{d}\|^2} + (\boldsymbol{d}\cdot\boldsymbol{d}')\dfrac{\|\boldsymbol{d}\|^2[I] - 2\boldsymbol{d}\boldsymbol{d}^T}{\|\boldsymbol{d}\|^4}\right) & -\dfrac{1}{\Delta t}\dfrac{\boldsymbol{d}\boldsymbol{d}^T}{\|\boldsymbol{d}\|^2} \end{bmatrix} \tag{11}$$

To implement another type of filter for state-estimation comparison, a square-root unscented Kalman (UKF) filter is implemented using the same formulation. The implementation of this filter is denoted as EKF or SR-UKF according to the algorithm used. The SR-UKF has no need for partial derivative calculation, which simplifies code by limiting the number of equations implemented seen in Eq. (11) and is used routinely for attitude determination [35]. As shown in Ref. [36], the UKF uses $\alpha = 0.02$ as a constant determining the spread of the sigma points. The prior knowledge of the probability distribution of the state is set with $\beta = 2$ (which is optimal for Gaussian distributions).

The challenge with this filter is that the algorithm creates a sun-heading rate $\boldsymbol{d}'$ estimate at first by assuming it is fully observable, and then it uses a projection to force the unobservable velocity component to be zero. Of interest is a filter that directly addresses this partial observability, and analyse how this new filter of interest performs relative to these previous filters.

IV. Switching Filters

This section derives the new switch-filter formulation (labeled "switch-EKF" and "switch-SRUKF" in the numerical simulations). This novel kinematic formulation uses the ability to switch between two frames to avoid singularities of the heading vector parameterization.

A. Frame Definitions

The switching filter attempts to avoid subtracting any terms from the estimate rate vector while still enforcing the unobservable rate component is zero. To do this, an appropriate sensor frame $\mathcal{S}\colon\{\hat{\boldsymbol{s}}_1, \hat{\boldsymbol{s}}_2, \hat{\boldsymbol{s}}_3\}$ must be defined as pictured in Fig. 3 alongside the body frame $\mathcal{B}\colon\{\hat{\boldsymbol{b}}_1, \hat{\boldsymbol{b}}_2, \hat{\boldsymbol{b}}_3\}$.

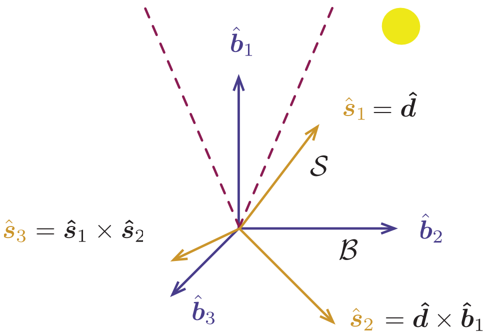

Fig. 3 Frame built off the body frame for switch filters.

To not track the rate component alongside the sun-line direction, a frame is defined such that the sun-line direction is one of the basis vectors. Without loss of generality, the sun-heading measurement direction $\boldsymbol{d}$ is chosen to be the aligned with the first base vector $\hat{\boldsymbol{s}}_1$:

$$\hat{\boldsymbol{s}}_1 = \frac{\boldsymbol{d}}{|\boldsymbol{d}|} \tag{12}$$

Thus, the rate component about $\hat{\boldsymbol{s}}_1$ is unobservable. The second and third $\mathcal{S}$-frame base vectors are arbitrary because any choice keeps the unobservable rate component along $\hat{\boldsymbol{s}}_1$. A simple choice is to define

$$\hat{\boldsymbol{s}}_2 = \frac{\hat{\boldsymbol{s}}_1 \times \hat{\boldsymbol{b}}_1}{|\hat{\boldsymbol{s}}_1 \times \hat{\boldsymbol{b}}_1|} \tag{13}$$

$$\hat{\boldsymbol{s}}_3 = \hat{\boldsymbol{s}}_1 \times \hat{\boldsymbol{s}}_2 \tag{14}$$

The problem that arises is the singularity that occurs when $\hat{\boldsymbol{b}}_1$ and $\boldsymbol{d}$ are aligned because this switch frame $\mathcal{S}$ is then undefined. To avoid this singularity, an alternate sensor frame $\bar{\mathcal{S}}$ is defined that also has the first base vector aligned with the sun-heading direction $\boldsymbol{d}$. This approach is similar in spirit to how the QUEST attitude estimation algorithm [37] avoids a singularity by switching between two kinematic descriptions, or how the modified Rodrigues parameters switch between two alternate attitude representations [25,28]: the underlying idea being that, when approaching an ill-defined frame $\mathcal{S}$ definition, a second frame $\bar{\mathcal{S}}$ is used. This frame $\bar{\mathcal{S}} = \{\hat{\bar{\boldsymbol{s}}}_1 = \hat{\boldsymbol{s}}_1, \hat{\bar{\boldsymbol{s}}}_2, \hat{\bar{\boldsymbol{s}}}_3\}$ cannot be singular at the same time as $\mathcal{S}$: it uses the same first vector but constructs $\hat{\bar{\boldsymbol{s}}}_2$ using $\hat{\boldsymbol{b}}_2$ of the body frame. The last vector, once again, completes the orthonormal frame:

$$\hat{\bar{\boldsymbol{s}}}_2 = \frac{\hat{\boldsymbol{s}}_1 \times \hat{\boldsymbol{b}}_2}{|\hat{\boldsymbol{s}}_1 \times \hat{\boldsymbol{b}}_2|} \tag{15}$$

$$\hat{\bar{\boldsymbol{s}}}_3 = \hat{\boldsymbol{s}}_1 \times \hat{\bar{\boldsymbol{s}}}_2 \tag{16}$$

By switching between the $\mathcal{S}$ and $\bar{\mathcal{S}}$ frames, the kinematic singularities are always avoided. The perpendicularity of $\hat{\boldsymbol{b}}_1$ and $\hat{\boldsymbol{b}}_2$ results in either $\mathcal{S}$ or $\bar{\mathcal{S}}$ being nonsingular at all times.

The switching strategy is therefore to define a cone around the body frame axis in use, and to switch between the frames when the heading enters the cone, as pictured in Fig. 3. In this implementation, whenever the sun line $\boldsymbol{d}$ gets within a cone of 30 deg of $\hat{\boldsymbol{b}}_1$, the frame is switched to $\bar{\mathcal{S}}$, which is not singular because the body vectors are orthonormal. Similarly, when $\boldsymbol{d}$ approaches $\hat{\boldsymbol{b}}_2$, the frame is switched back to $\mathcal{S}$.

Because the two frames share the sun-line vector $\boldsymbol{d}$, both frames have the unobservable rate component along the first axis. Furthermore, the sun heading to be estimated is the same first base vector. The vector components are mapped between the body frame $\mathcal{B}$ and the two sensor frames ($\mathcal{S}$ and $\bar{\mathcal{S}}$) using the following direction cosine matrices or DCMs:

$$\mathcal{BS} = \begin{bmatrix} {}^{\mathcal{B}}\hat{\boldsymbol{s}}_1 & {}^{\mathcal{B}}\hat{\boldsymbol{s}}_2 & {}^{\mathcal{B}}\hat{\boldsymbol{s}}_3 \end{bmatrix} \tag{17a}$$

$$\mathcal{B}\bar{\mathcal{S}} = \begin{bmatrix} {}^{\mathcal{B}}\hat{\bar{\boldsymbol{s}}}_1 & {}^{\mathcal{B}}\hat{\bar{\boldsymbol{s}}}_2 & {}^{\mathcal{B}}\hat{\bar{\boldsymbol{s}}}_3 \end{bmatrix} \tag{17b}$$

$$\bar{\mathcal{S}}\mathcal{S} = [\mathcal{B}\bar{\mathcal{S}}]^T[\mathcal{BS}] \tag{17c}$$

Given a sun-heading vector estimate $\boldsymbol{d}$, all these base vectors are know at any given time.

B. Filter Kinematics

The body rate relative to the inertial frame is projected onto the $\mathcal{B}$ frame and the $\mathcal{S}$ frame:

$$\boldsymbol{\omega}_{\mathcal{BN}} = \omega_1\hat{\boldsymbol{b}}_1 + \omega_2\hat{\boldsymbol{b}}_2 + \omega_3\hat{\boldsymbol{b}}_3 \tag{18}$$

$$= \omega_{s,1}\hat{\boldsymbol{s}}_1 + \omega_{s,2}\hat{\boldsymbol{s}}_2 + \omega_{s,3}\hat{\boldsymbol{s}}_3 \tag{19}$$

The rates of $\mathcal{S}$ relative to the body and inertial frames are related as such: $\boldsymbol{\omega}_{\mathcal{SN}} - \boldsymbol{\omega}_{\mathcal{SB}} = \boldsymbol{\omega}_{\mathcal{BN}}$. The first vector of $\mathcal{S}$ is the sun heading that is considered to be constant in the inertial frame over the period of time required for heading determination. Hence, the only component of $\boldsymbol{\omega}_{\mathcal{SN}}$ that can vary is the rate about the sun heading: ${}^{\mathcal{S}}\boldsymbol{\omega}_{\mathcal{SN}} = {}^{\mathcal{S}}[\boldsymbol{\omega}_{\mathcal{SN}} \cdot \hat{\boldsymbol{d}} \quad 0 \quad 0]^T$. Because the sun-line rotation is impossible to extract from CSS measurements, the spacecraft rotation about the sun-heading axis is set to zero by the filter. This rate component is fundamentally unobservable, and it is therefore set to zero.

In Eq. (19), the previous statement leads to $\omega_{s,1} = 0$. It is important to note that no spacecraft rotation assumption is made; rather, the filter zeros the component that it cannot observe geometrically. The body-rate vector with the previous assumption is defined as follows:

$$\boldsymbol{\omega}^* = \boldsymbol{\omega}_{\mathcal{BN}}(\omega_{s,1} = 0) = \omega_{s,2}\hat{\boldsymbol{s}}_2 + \omega_{s,3}\hat{\boldsymbol{s}}_3 \tag{20}$$

$${}^{\mathcal{S}}\boldsymbol{\omega}^* = {}^{\mathcal{S}}[0 \quad \omega_{s,2} \quad \omega_{s,3}]^T \tag{21}$$

Zeroing this term prevents all motion of the $\mathcal{S}$ frame relative to the inertial frame because it was the only possible motion given $\dot{\boldsymbol{d}} = \boldsymbol{0}$. Hence, as far as the filter can see, Eq. (21) leads to $\boldsymbol{\omega}_{\mathcal{SN}} = \boldsymbol{0}$; and the rate relationship becomes $-\boldsymbol{\omega}_{\mathcal{SB}} = \boldsymbol{\omega}^*$. No spacecraft rotation assumption is made, but the kinematics of the filter are simplified, given the constraints of observability. The following is a summary:

1) Because $\dot{\boldsymbol{d}} = \boldsymbol{0}$ and $\hat{\boldsymbol{d}}$ is the first component of $\mathcal{S}$, $\boldsymbol{\omega}_{\mathcal{SN}}$ can only rotate about $\hat{\boldsymbol{d}}$.

2) this rotation about $\hat{\boldsymbol{d}}$ is precisely the rotation that cannot be observed by the spacecraft. Without any possible knowledge of this motion, the switch filters set this motion to zero in the kinematics.

3) In the filter kinematics, this zeros $\boldsymbol{\omega}_{\mathcal{SN}}$; and $\boldsymbol{\omega}_{\mathcal{SN}} - \boldsymbol{\omega}_{\mathcal{SB}} = \boldsymbol{\omega}_{\mathcal{BN}}$ therefore becomes $-\boldsymbol{\omega}_{\mathcal{SB}} = \boldsymbol{\omega}^*$, where $\boldsymbol{\omega}^*$ also zeros the rate about the sun heading.

The fact that the filter sets the nonobservable component to zero is ideal for control applications: this prevents a control solution from applying any correction to an axis that can fundamentally not be observed.

The filter state is therefore $\boldsymbol{X} = [{}^{\mathcal{B}}\boldsymbol{d} \quad \omega_{s,2} \quad \omega_{s,3}]^T$, and the kinematics are given by

$$\boldsymbol{X}' = \boldsymbol{F}(\boldsymbol{X}) = \begin{bmatrix} {}^{\mathcal{B}}\boldsymbol{d}' \\ \dot{\omega}_{s,2} \\ \dot{\omega}_{s,3} \end{bmatrix} = \begin{bmatrix} -{}^{\mathcal{B}}\boldsymbol{\omega}^* \times {}^{\mathcal{B}}\boldsymbol{d} \\ 0 \\ 0 \end{bmatrix} = \begin{bmatrix} -[\mathcal{BS}] \, {}^{\mathcal{S}}\begin{bmatrix} 0 \\ \omega_{s,2} \\ \omega_{s,3} \end{bmatrix} \times {}^{\mathcal{B}}\boldsymbol{d} \\ 0 \\ 0 \end{bmatrix} \tag{22}$$

$$[A] = \left[\frac{\partial \boldsymbol{F}(\boldsymbol{d}, t_i)}{\partial \boldsymbol{X}}\right] = \begin{bmatrix} -[{}^{\mathcal{B}}\tilde{\boldsymbol{\omega}}^*] & -[\tilde{\boldsymbol{d}}][\,{}^{\mathcal{B}}\hat{s}_2 \quad {}^{\mathcal{B}}\hat{s}_3\,] \\ [0]_{2\times 3} & [0]_{2\times 2} \end{bmatrix} \tag{23}$$

The 3×2 matrix in the dynamics matrix corresponds to the truncated DCM $[\mathcal{B}S]$, and $\dot{\omega}$ is the time derivative of the scalar component ω. Equation (23) shows the zeroed sun-line rotation component in the filter kinematics.

This formulation leads to simple kinematics, which is much simpler than those of the filter that subtracts the unobservable states yet can actually estimate the two observable vector components of the rate instead of using past estimates of $\boldsymbol{d}$. In regard to the SR-UKF version of this filter, the same coefficients are used: $\alpha = 0.02$, and $\beta = 2$.

C. Switching Frames

The challenge that comes with the novelty of using two frames for the kinematics is switching between them. The new states $\bar{\boldsymbol{X}}$ and covariance $[\bar{P}]$ after the switch are

$$\bar{\boldsymbol{X}} = [W]\boldsymbol{X}[\bar{P}] = [W][P][W]^T \tag{24}$$

where $\boldsymbol{X}$ and $[P]$ represent the state and covariance in the $\bar{\mathcal{S}}$ frame. The $[W]$ matrix maps the rate components from the $\mathcal{S}$ frame to the $\bar{\mathcal{S}}$ frame when a switch occurs. The matrix $[W]$ is derived with

$$[W] = \begin{bmatrix} [I]_{3\times 3} & [0]_{3\times 2} \\ [0]_{2\times 3} & \begin{bmatrix} \hat{\bar{\boldsymbol{s}}}_2 \cdot \hat{\bar{\boldsymbol{s}}}_2 & \hat{\bar{\boldsymbol{s}}}_2 \cdot \hat{\bar{\boldsymbol{s}}}_3 \\ \hat{\bar{\boldsymbol{s}}}_3 \cdot \hat{\bar{\boldsymbol{s}}}_2 & \hat{\bar{\boldsymbol{s}}}_3 \cdot \hat{\bar{\boldsymbol{s}}}_3 \end{bmatrix} \end{bmatrix} \tag{25}$$

using the previously computed $\mathcal{S}$ and $\bar{\mathcal{S}}$ frame base vectors. The sun-heading vector $\boldsymbol{d}$ is unmodified, whereas the rates are rotated into the switched frame. This equation assumes the switch is going from the $\mathcal{S}$ frame to $\bar{\mathcal{S}}$ (the reciprocal is equivalent), and

$$\begin{bmatrix} \hat{\bar{\boldsymbol{s}}}_2 \cdot \hat{\bar{\boldsymbol{s}}}_2 & \hat{\bar{\boldsymbol{s}}}_2 \cdot \hat{\bar{\boldsymbol{s}}}_3 \\ \hat{\bar{\boldsymbol{s}}}_3 \cdot \hat{\bar{\boldsymbol{s}}}_2 & \hat{\bar{\boldsymbol{s}}}_3 \cdot \hat{\bar{\boldsymbol{s}}}_3 \end{bmatrix} \tag{26}$$

corresponds to the bottom-left 2×2 submatrix of $[\bar{\mathcal{S}}\mathcal{S}]$. Equation (25) therefore provides a first-order frame change for the covariance, allowing for the filter to continue its state estimation nominally.

D. Process Noise for Switch EKF

Another nuance that arises when writing EKFs is the process noise formula. This is addressed by deriving the $[\Gamma]$ matrix that transports the noise to the state space, given the new state vector. The time update of the error covariance matrix $[P]$ from time t_k to t_{k+1} ($\Delta t = t_{k+1} - t_k$) is

$$[P]_{k+1} = [\Phi](t_{k+1}, t_k)[P]_k[\Phi](t_{k+1}, t_k)^T + [\Gamma](t_{k+1}, t_k)[Q][\Gamma](t_{k+1}, t_k)^T \tag{27}$$

$$[\Gamma](t_{k+1}, t_k) = \int_{t_k}^{t_{k+1}} [\Phi](t_{k+1}, \tau)[B](\tau)\,\mathrm{d}\tau \tag{28}$$

where the process noise matrix $[Q]$ is added via the $[\Gamma]$ matrix defined in Eq. (28) [27]. The $[B]$ matrix seen in the integral maps the process noise only on the accelerations, meaning that

$$[B] = \begin{bmatrix} [0]_{3\times 3} \\ [I]_{3\times 3} \end{bmatrix}$$

when there are six states.

In the earlier filters (the EKF and the SR-UKF), the second half of the state vector is a direct derivative of the sun-heading vector. Regarding state noise compensation, this allows the following approximation:

$$[\Gamma](t_{k+1}, t_k) = \Delta t \begin{bmatrix} \frac{\Delta t}{2}[I]_{3\times 3} \\ [I]_{3\times 3} \end{bmatrix} \tag{29}$$

along with the fact that measurements are received frequently with regard to the evolution of the dynamics.

This does not hold for the switch filter because $[\Phi]$ is a 5×5 matrix, hence the development of the following section. To simplify the notation of partials in this section, $\bar{\boldsymbol{\omega}}$ will represent the 2×1 matrix $[\,\omega_{s,2} \quad \omega_{s,3}\,]^T$:

$$[\Phi](t_{k+1}, \tau) = \begin{bmatrix} [\Phi_1]_{3\times 3} & [\Phi_2]_{3\times 2} \\ [\Phi_3]_{2\times 3} & [\Phi_4]_{2\times 2} \end{bmatrix} = \begin{bmatrix} \dfrac{\partial \boldsymbol{d}(t_{k+1})}{\partial \boldsymbol{d}(\tau)} & \dfrac{\partial \boldsymbol{d}(t_{k+1})}{\partial \bar{\boldsymbol{\omega}}(\tau)} \\ \dfrac{\partial \bar{\boldsymbol{\omega}}(t_{k+1})}{\partial \boldsymbol{d}(\tau)} & \dfrac{\partial \bar{\boldsymbol{\omega}}(t_{k+1})}{\partial \bar{\boldsymbol{\omega}}(\tau)} \end{bmatrix} \tag{30}$$

Equation (30) uses the fact that

$$[\Phi](t_{k+1}, \tau) = \frac{\partial \boldsymbol{X}(t_{k+1})}{\partial \boldsymbol{X}(\tau)}$$

and that $\boldsymbol{X} = [\,\boldsymbol{d} \quad \bar{\boldsymbol{\omega}}\,]^T$. With this, Eq. (29) can be rewritten:

$$\begin{aligned} [\Gamma](t_{k+1}, t_k) &= \int_{t_k}^{t_{k+1}} \begin{bmatrix} [\Phi_1]_{3\times 3} & [\Phi_2]_{3\times 2} \\ [\Phi_3]_{2\times 3} & [\Phi_4]_{2\times 2} \end{bmatrix} \begin{bmatrix} [0]_{3\times 3} \\ [I]_{3\times 3} \end{bmatrix} \mathrm{d}\tau \\ &= \int_{t_k}^{t_{k+1}} \begin{bmatrix} [\Phi_2]_{3\times 2} \\ [\Phi_4]_{2\times 2} \end{bmatrix} \mathrm{d}\tau \end{aligned} \tag{31}$$

These submatrices of the state transition matrix now need to be approximated. As before, assuming dense tracking data,

$$[\Phi_4]_{2\times 2} = \frac{\partial \bar{\boldsymbol{\omega}}(t_{k+1})}{\partial \bar{\boldsymbol{\omega}}(\tau)} \approx [I]_{2\times 2}$$

Then, define the $[J]$ matrix as

$$[J] = \begin{bmatrix} [0]_{1\times 2} \\ [I]_{2\times 2} \end{bmatrix} \tag{32}$$

The rate notations are reconciled through ${}^{\mathcal{S}}\boldsymbol{\omega}^* = [J]\bar{\boldsymbol{\omega}}$. Without specifying a frame, the propagation function yields

$$\boldsymbol{d}_{k+1} - \boldsymbol{d}_\tau = (t_{k+1} - \tau)[\tilde{\boldsymbol{d}}_\tau]\boldsymbol{\omega}^* \tag{33}$$

By then moving into the body frame,

$$\frac{\partial {}^{\mathcal{B}}\boldsymbol{d}(t_{k+1})}{\partial \bar{\boldsymbol{\omega}}(\tau)} = (t_{k+1} - \tau)[{}^{\mathcal{B}}\tilde{\boldsymbol{d}}_\tau][\mathcal{B}\mathcal{S}][J] \tag{34}$$

$$[\Phi_2]_{3\times 2} = (t_{k+1} - \tau)[{}^{\mathcal{B}}\tilde{\boldsymbol{d}}_\tau][\,{}^{\mathcal{B}}\hat{\boldsymbol{s}}_2 \quad {}^{\mathcal{B}}\hat{\boldsymbol{s}}_3\,] \tag{35}$$

Therefore, assuming the state does not vary over the time between two updates, $[\Phi_2]_{3\times 2}$ can be integrated to approximate $[\Gamma]$:

$$[\Gamma](t_{k+1}, t_k) = \int_{t_k}^{t_{k+1}} \begin{bmatrix} [\Phi_2]_{3\times 2} \\ [\Phi_4]_{2\times 2} \end{bmatrix} \mathrm{d}\tau = \Delta t \begin{bmatrix} \frac{\Delta t}{2}\left[{}^{\mathcal{B}}\tilde{\boldsymbol{d}}_k\right][\,{}^{\mathcal{B}}\tilde{\boldsymbol{s}}_2 \; {}^{\mathcal{B}}\tilde{\boldsymbol{s}}_3\,] \\ [I]_{2\times 2} \end{bmatrix} \tag{36}$$

This leads to the new $[\Gamma]$ matrix in Eq. (36), which is used for state noise compensation.

V. Simulation and Results

Five filters were developed out of the three kinematic formulations described in the previous section. The subtraction of the unobservable states formulation is written into a square-root unscented Kalman filter and an extended Kalman filter. The formulation that only estimates the sun-line direction is implemented in an EKF (sun-line-EKF). Finally, the novel formulation is written in an EKF and a SR-UKF (switch-EKF and switch-SRUKF).

The simulation used is created using the Basilisk software package [1,38,39]. All runs simulate a tumbling spacecraft in deep space, at 1 AU from the sun. The problem assumes that the time needed for control is much smaller than the time needed to orbit around the sun, meaning that $\dot{\boldsymbol{d}} \approx \boldsymbol{0}$. The satellite is therefore not put on orbit around the sun but kept in a constant position in the inertial frame. The general simulation parameters used for more are summarized in Table 3.

Table 3 Initial condition dispersions

Parameter	$\boldsymbol{\sigma}_{\mathcal{BN}}(t_0)$	$\boldsymbol{\omega}(t_0)$, deg/s
Fast distribution	$\mathcal{U}[0, 2\pi]$	$\pm\mathcal{N}[0.45, 0.55]$
Nominal distribution	$\mathcal{U}[0, 2\pi]$	$\pm\mathcal{N}[0.05, 0.15]$
Slow distribution	$\mathcal{U}[0, 2\pi]$	$\pm\mathcal{N}[0.001, 0.01]$

Table 4 State noise compensation (SNC)[a]

Filter	Sun-line-EKF	EKF	SR-UKF	Switch-EKF	Switch-UKF
SNC on $\boldsymbol{d}$	10^{-2}	N/A	10^{-3}	N/A	10^{-3}
SNC on rates	N/A	$2 \cdot 10^{-4}$	$2 \cdot 10^{-4}$	$8 \cdot 10^{-4}$	$8 \cdot 10^{-4}$

[a] N/A denotes “not applicable.”

For all of the results, the filters retain the same process noise, which is listed in Table 4. These values are chosen by reducing the postfit residuals to noise at slow spacecraft rotation rates, which is the most common state for a controlled spacecraft. It is then desirable to test the robustness of these filters as such in order to determine which ones are the best overall.

First, the switch filters are examined to ensure proper implementation and behavior. Second, all the implementations are compared in a scenario in order to observe overall performance and covariance behavior. Finally, the best filters are run in a diverse set of simulations with low and high observability to show the best overall performing filters.

A. Switch-Filter Results

This subsection examines the implementation of the switch-EKF and switch-SRUKF. These results are created using the simulation parameters of Table 1, which initialize the spacecraft in a mild tumble. Figure 4 shows the state error and 3-σ covariance bounds for the switch-EKF filter, whereas Fig. 5 shows the switch-SRUKF. Both these filters perform well because the state errors are within the covariance (except for an outlier measurement) bounds and unbiased: this is seen in Table 5, where the means and standard deviation map well onto the input $\mathcal{N}(0, 0.017)$ values.

This is seen more specifically with the postfit residuals seen in Fig. 6 from the switch-SRUKF run. The measurements are brought down to noise, with the expected standard deviations, which is expected because the simulation does not have any unmodeled forces acting on the spacecraft. The switch-EKF postfits are not displayed but are nearly identical and provide confidence that the filter is working optimally. The gaps in the postfits correspond to changing the number of sensors that can observe the sun. With this CSS pyramid, there are always two active sensors, with only brief passages down to three or four sensors.

Figure 7 shows one of the novel components of the switch filters: direct body-rate estimation. The filters can be seen tracking the true body rates in the $\mathcal{S}$ frame (disregarding the unobservable component

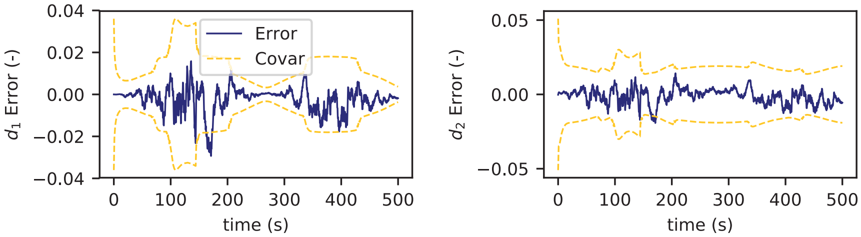

a) First heading component

b) Second heading component

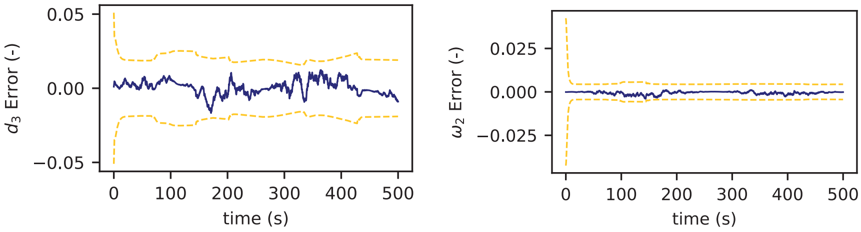

c) Third heading component

d) ω_2 component

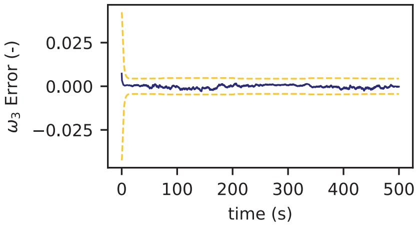

e) ω_3 component

Fig. 4 State error and covariance (Covar) plots of switch-EKF, with FOV = 85 deg.

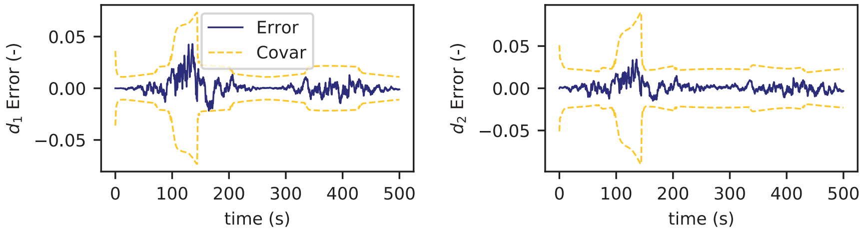

a) First heading component

b) Second heading component

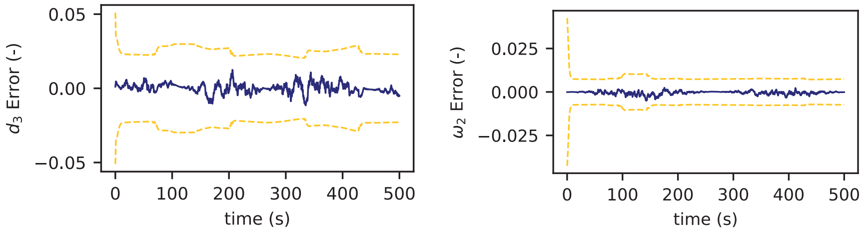

c) Third heading component

d) ω_2 component

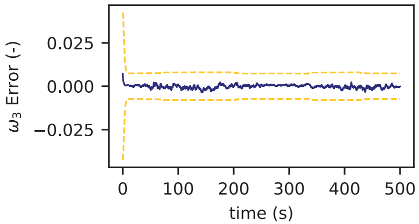

e) ω_3 component

Fig. 5 State error and covariance plots of switch-SRUKF, with FOV = 85 deg.

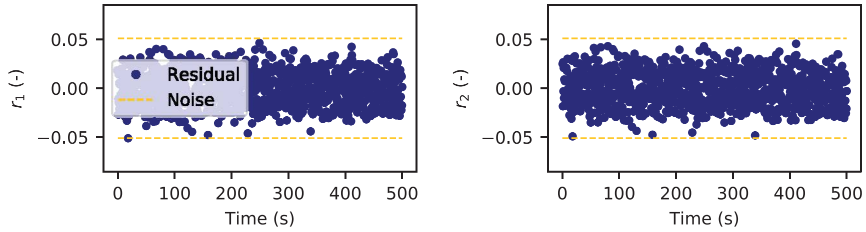

a) First active CSS

b) Second active CSS

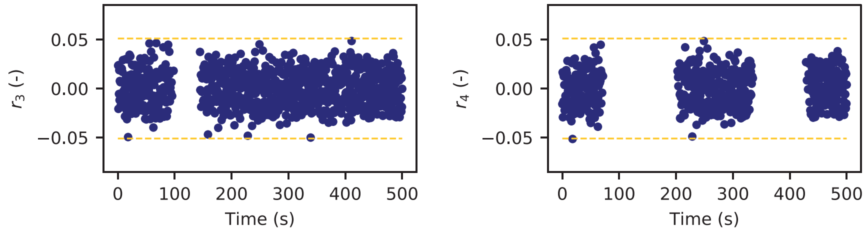

c) Third active CSS

d) Fourth active CSS

Fig. 6 Postfit residuals for switch-SRUKF, with FOV = 85 deg.

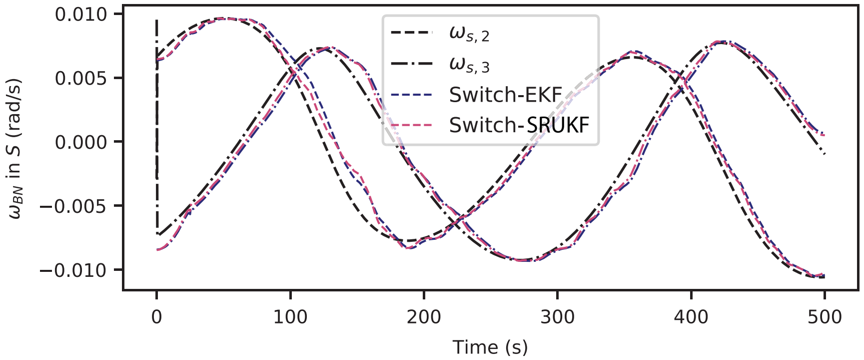

Fig. 7 Switch filters tracking the rates in the $\mathcal{S}$ frame.

Table 5 Postfit residuals in nominal case, with FOV = 85 deg

Filter	Statistics	Observation 1	Observation 2	Observation 3	Observation 4
Sun-line-EKF	Means	−0.0007	0.0023	−0.009	0.0139
	Standard deviations	0.0331	0.0313	0.0508	0.0351
EKF	Means	−0.0019	0.0004	0.0001	−0.0021
	Standard deviations	0.0181	0.0198	0.0186	0.0182
SR-UKF	Means	0.0013	0.0027	0.0029	0.0096
	Standard deviations	0.0187	0.0244	0.0344	0.0692
Switch-EKF	Means	−0.0026	−0.0004	0.0006	−0.0012
	Standard deviations	0.0191	0.033	0.0356	0.0175
Switch-SRUKF	Means	0.0	0.001	0.0025	0.0096
	Standard deviations	0.0186	0.0243	0.0343	0.0692

that the filter ignores). Although just two components of this vector do not yet allow us to fully estimate the body rate without extra information, it proves that the filters are functioning. This plot also shows the filter starting off in the middle of the singularity (heading and body frame vector aligned), switching frames, and pursuing the estimation with no more singularities encountered. Furthermore, if additional headings were tracked and fused, full body-rate estimation would be achievable.

B. General Results

The simulation runs the filters with good and low-quality measurements. As described previously, the filters are calibrated for their postfit residuals to be noise at low speeds. With a field of view of 85 deg on each sensor, the problem has good observability, as seen in Fig. 2b. Table 5 shows the postfit residuals' means and standard deviations for each of the activated devices. All the means are near zero, which indicates no biases; whereas standard deviations are very close to the measurement noise of the instruments. The specific results are plotted in this section, as well as the lower-quality measurements (Fig. 2a):

$$\dot{\boldsymbol{d}} = \boldsymbol{0} = \boldsymbol{d}' + \boldsymbol{\omega}_{\mathcal{B}\mathcal{N}} \times \boldsymbol{d} \tag{37}$$

These filters are compared by plotting their off-pointing in degrees and the norm of the error on $\boldsymbol{d}'$ in Fig. 8. For the switch filters (which do not estimate $\boldsymbol{d}'$), the rate is mapped back using the transport theorem as seen in Eq. (37). Knowledge of $\boldsymbol{d}$ and $\boldsymbol{d}'$ does not allow identification of the body rate uniquely due to the rank deficiency of the cross operator. Hence, the current estimate of the sun heading and the observable components of the body rate are used to compute $\boldsymbol{d}'$. The data are smoothed using a Savitzky–Golay algorithm [40] in order to differentiate between the curves more easily. This algorithm does lead to spikes at the end of Figs. 8a and 8b.

Figure 8a shows the off-pointing errors of all the filters, and Fig. 8b displays the rate error. Tables 6 and 7 show the computed rms errors for the filters in both the 85 and 60 deg field-of-view (FOV) cases. The results show that the switch filter outperforms the others: both in rate and heading estimation. Due to the process noise on the body rates, the switch filter sun-heading errors are slightly higher than some other results at low-speed tumbles. Yet, at these speeds, all the filters provide errors that are less than half of a degree off.

C. Results in Diverse Set of Cases

In this subsection, a set of initial conditions is run to show the overall improved performance of the switch filters. The goal of this section is to show the performance of the switch filter given different

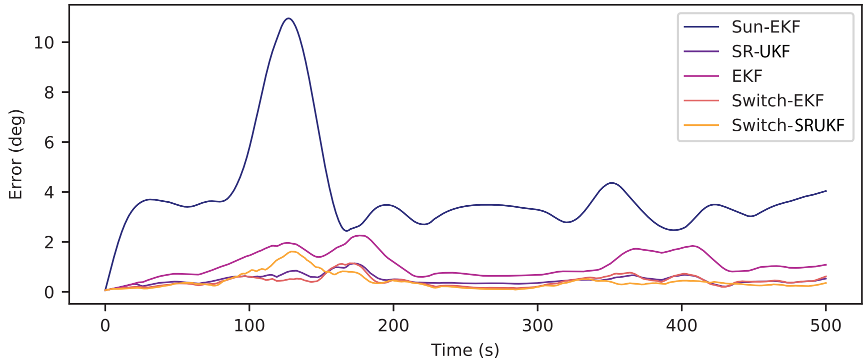

a) Pointing miss angle (in degrees)

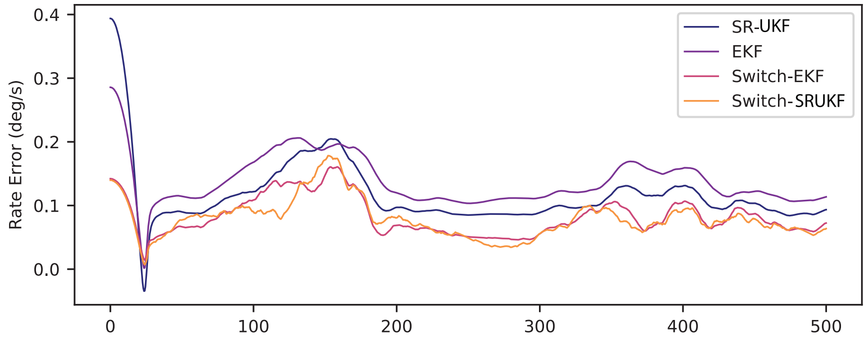

b) $\boldsymbol{d}'$ norm error

Fig. 8 Comparative performance of the filters, with FOV = 85 deg.

Table 6 RMS errors from truth, with FOV = 85 deg

Filter	Sun-line-EKF	EKF	SR-UKF	Switch-EKF	Switch-UKF
d rms pointing error, deg	2.388	0.678	0.315	0.304	0.334
d′ rms error,	N/A	0.089	0.087	0.055	0.056

Table 7 RMS errors from truth, with FOV = 60 deg

Filter	Sun-line-EKF	EKF	SR-UKF	Switch-EKF	Switch-SRUKF
d rms pointing error, deg	7.651	4.695	3.003	3.568	2.151
d′ rms error	N/A	0.168	0.139	0.17	0.117

initial conditions, tumbles, and sensor field of views. The dispersed parameters are the initial conditions to the spacecraft tumble: initial attitude and attitude rate. This study allows us to ensure that the better performance of a specific filter is not attributed to favorable initial conditions. The different initial conditions are applied in three different tumble scenarios: the first is a slowly rotating spacecraft scenario and is the scenario to which all the filters are calibrated; the second scenario is a nominal rotation, akin to a slow maneuver; the third scenario is a fast rotation spacecraft similar to a tumble. The dispersions applied in each of these cases are listed in Table 3.

Figure 9 shows the results of 10 random runs in the high-observability scenario. For clarity, the sun-line-EKF filter (which was not performing as well as the others) is removed from this analysis. This allows for a more focused analysis on the best filters. These runs show that the switch-UKF performs consistently better than its competitors. At slow speeds, the difference between all the filters is hard to gauge because this is the run that calibrated the process noise. It does seem that, despite overall excellent performance, this is the only realm where the switch formulations do not estimate sun heading better than the others. Yet, the switch formulations and, more notably, the switch-SRUKF handle the faster spacecraft rates considerably better than the other filters.

Figure 10 shows the results of 10 runs in the low-observability scenario. The scenario at low speed also contains very low-observability scenarios where no more than two or three sensors are activated, which yield high errors. With fewer measurements, all the filters perform less well; yet, once again, the switch-SRUKF consis-

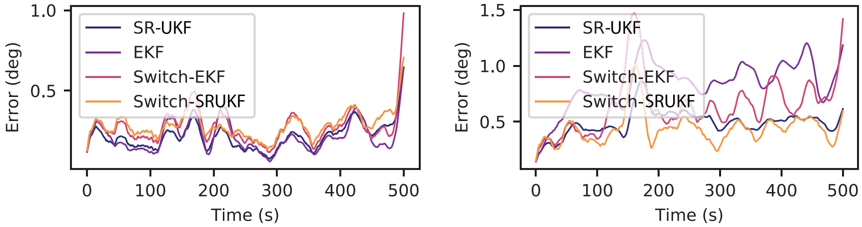

a) Slow tumble scenario **b) Nominal tumble scenario**

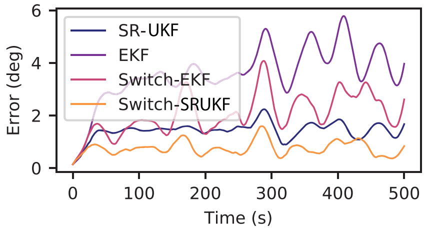

c) Fast tumble scenario

Fig. 9 Average of 10 simulations, with FOV = 85 deg.

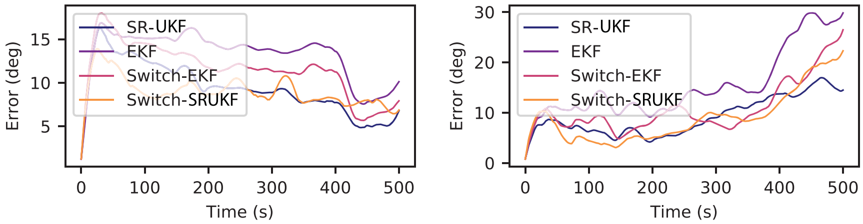

a) Slow tumble scenario **b) Nominal tumble scenario**

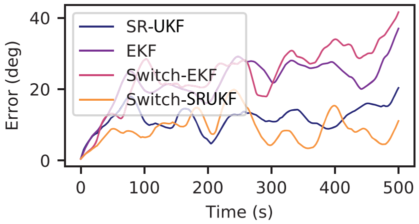

c) Fast tumble scenario

Fig. 10 Average of 10 simulations, with FOV = 60 deg.

tently yields the smallest heading errors. This shows the value of this formulation: in the event of component failure, the switch filters will provide consistently better sun-heading estimates. This contributes to the robustness of the attitude determination system.

VI. Conclusions

This paper shows the comparative performances of several filters and formulations attempting to solve the CSS-only heading determination problem. To provide a better and more robust algorithm, two kinematic representations (akin to the two sets of MRPs) are implemented and the algorithm switches between them to avoid singularities. This leads to a change in the process noise derivation for an EKF, and it requires a switch in the covariance on the rate states as well. At slow rates, all filters perform approximately the same. Then, at higher rates, the switch formulations provide better results than all other filters implemented on the problem. Through these more complex kinematics, the switch formulations analytically extract rate unobservability. This provides confidence in regard to the numerics of the filters as well as the overall state error.

More specifically, the switch-SRUKF performs the best all around: whether the CSSs have a narrow or wide field of view. The nonlinear propagation of sigma points combined with the novel switch formulation provides a good propagation step and allows for full utilization of the measurements despite inherent unobservability. In fact, switch filters have removed the problem of the unobservable rate component from the estimation entirely. If combined with wide field-of-view CSS instruments, it does not suffer from any observability issues: numerical or analytical.

Acknowledgment

This work was presented as Paper 2019 at the 29th AAS/AIAA Space Flight Mechanics Meeting in Maui, Hawaii, 13–17 January 2019.

References

[1] Lefferts, E. J., Markley, F. L., and Shuster, M. D., "Kalman Filtering for Spacecraft Attitude Estimation," *20th Aerospace Sciences Meeting*, AIAA Paper 1982-0070, 1982.
https://doi.org/10.2514/6.1982-70

[2] Crassidis, J. L., Markley, F. L., and Cheng, Y., "Survey of Nonlinear Attitude Estimation Methods," *Journal of Guidance, Control, and Dynamics*, Vol. 30, No. 1, 2007, pp. 12–28.
https://doi.org/10.2514/1.22452

[3] Nguyen, T., Cahoy, K., and Marinan, A., "Attitude Determination for Small Satellites with Infrared Earth Horizon Sensors," *Journal of Spacecraft and Rockets*, Vol. 55, No. 6, 2018, pp. 1466–1475.
https://doi.org/10.2514/1.A34010

[4] de Ruiter, A. H. J., Tran, L., Kumar, B. S., and Muntyanov, A., "Sun Vector-Based Attitude Determination of Passively Magnetically Stabilized Spacecraft," *Journal of Guidance, Control, and Dynamics*, Vol. 39, No. 7, 2016, pp. 1551–1562.
https://doi.org/10.2514/1.G001757

[5] Chiang, R. Y., "Star Tracker Rate Estimation with Kalman Filter Enhancement," *AIAA Guidance, Navigation, and Control (GNC) Conference*, AIAA Paper 2013-5024, 2013.
https://doi.org/10.2514/6.2013-5024

[6] Gates, R. F., and McAloon, K. J., "Precision Star Tracker Utilizing Advanced Techniques and Materials," *Journal of Spacecraft and Rockets*, Vol. 13, No. 10, 1976, pp. 594–599.
https://doi.org/10.2514/3.57123

[7] Lyons, M. G., and Debra, D. B., "A Reduced State Estimator for Orbital Heading Reference," *Journal of Spacecraft and Rockets*, Vol. 11, No. 2, 1974, pp. 97–100.
https://doi.org/10.2514/3.62015

[8] Pong, C. M., and Miller, D. W., "Reduced-Attitude Boresight Guidance and Control on Spacecraft for Pointing, Tracking, and Searching," *Journal of Guidance, Control, and Dynamics*, Vol. 38, No. 6, 2015, pp. 1027–1035.
https://doi.org/10.2514/1.G000264

[9] Allgeier, S., Mahin, M., and Fitz-Coy, N., "Design and Analysis of a Coarse Sun Sensor for Pico-Satellites," AIAA Paper 2009-1837, 2009.
https://doi.org/10.2514/6.2009-1837

[10] Hsiao, F.-Y., Chou, W.-T., Cato, T., and Rebelo, C., "Coarse Sun Acquisition Only with Sun Sensors for Micro Satellites," *25th AAS/AIAA Space Flight Mechanics Meeting Proceedings*, AAS Paper 15-319, Springfield, VA, 2015.

[11] Swei, S. S. M., Fusco, J. C., and Nakamura, R. H., "Design of Sun-Safe Controllers for Lunar Atmosphere and Dust Environment Explorer," *Journal of Guidance, Control, and Dynamics*, Vol. 39, No. 9, 2016, pp. 2022–2033.
https://doi.org/10.2514/1.G000270

[12] Markley, F. L., and Cheng, Y., "Wahba's Problem with One Dominant Observation," *Journal of Guidance, Control, and Dynamics*, Vol. 41, No. 10, 2018, pp. 2318–2323.
https://doi.org/10.2514/1.G003619

[13] Fusco, J., Swei, S. S.-M., and Nakamura, R., "Sun Safe Mode Controller Design for LADEE," AIAA Paper 2015-2011, 2015.
https://doi.org/10.2514/6.2015-2011

[14] Huston, R. L., "Twin-Gyro Attitude Control Systems," *Journal of Spacecraft and Rockets*, Vol. 3, No. 7, 1966, pp. 1136–1138.
https://doi.org/10.2514/3.28613

[15] Chheda, B., Crassidis, A., and Walter, W., "Attitude Estimation Using an Accelerometer and Rate Gyro Based Device," *AIAA Atmospheric Flight Mechanics Conference and Exhibit*, AIAA Paper 2006-6279, 2006.
https://doi.org/10.2514/6.2006-6279

[16] Crassidis, J. L., and Markley, F. L., "Three-Axis Attitude Estimation Using Rate-Integrating Gyroscopes," *Journal of Guidance, Control, and Dynamics*, Vol. 39, No. 7, 2016, pp. 1513–1526.
https://doi.org/10.2514/1.G000336

[17] Breckenridge, W. G., and Treder, A. J., "In-Flight Gyro Drift Rate Calibration on the Viking Orbiters," *Journal of Guidance, Control, and Dynamics*, Vol. 1, No. 6, 1978, pp. 433–439.
https://doi.org/10.2514/3.55806

[18] Mercker, T. H., and Akella, M. R., "Rigid-Body Attitude Tracking with Vector Measurements and Unknown Gyro Bias," *Journal of Guidance, Control, and Dynamics*, Vol. 34, No. 5, 2011, pp. 1474–1484.
https://doi.org/10.2514/1.53111

[19] Gioia, C. J., and Christian, J. A., "Gyro Bias Estimation Using Interior Star Angles for Manual Attitude Determination," *Journal of Spacecraft and Rockets*, Vol. 54, No. 2, 2017, pp. 513–522.
https://doi.org/10.2514/1.A33672

[20] Thakur, D., and Akella, M. R., "Gyro-Free Rigid-Body Attitude Stabilization Using Only Vector Measurements," *Journal of Guidance, Control, and Dynamics*, Vol. 38, No. 4, 2015, pp. 811–818.
https://doi.org/10.2514/1.G000623

[21] Yang, S., Akella, M. R., and Mazenc, F., "Immersion and Invariance Observers for Gyro-Free Attitude Control Systems," *Journal of Guidance, Control, and Dynamics*, Vol. 39, No. 11, 2016, pp. 2570–2577.
https://doi.org/10.2514/1.G002095

[22] Tsao, T., and Chiang, R., "Gyroless Transfer Orbit Sun Acquisition Using Only Wing Current Feedback," *AIAA Guidance, Navigation, and Control Conference*, AIAA Paper 2009-5944, 2009.
https://doi.org/10.2514/6.2009-5944

[23] O'Keefe, S. A., and Schaub, H., "Sun Heading Estimation Using Underdetermined Set of Coarse Sun Sensors," *AAS/AIAA Astrodynamics Specialists Conference*, AAS Paper 13-891, Springfield, VA, 2013.

[24] Chiang, R. Y., and Tsao, T., "Gyroless 3-Axis Sun Acquisition via Sun Sensors Only Unscented Kalman Filter Estimation," AIAA Paper 2013-5025, 2013.
https://doi.org/10.2514/6.2013-5025

[25] Schaub, H., and Junkins, J. L., "Stereographic Orientation Parameters for Attitude Dynamics: A Generalization of the Rodrigues Parameters," *Journal of the Astronautical Sciences*, Vol. 44, No. 1, 1996, pp. 1–19.

[26] O'Keefe, S. A., and Schaub, H., "On-Orbit Coarse Sun Sensor Calibration Sensitivity to Sensor and Model Error," *AAS/AIAA Space Flight Mechanics Meeting*, AAS Paper 15-392, Springfield, VA, 2015.

[27] Tapley, B., Schutz, B., and Born, G. H., "Fundamentals of Orbit Determination," *Statistical Orbit Determination*, Elsevier Academic, New York, 2004, pp. 159–284, Chap. 4.
https://doi.org/10.1016/B978-012683630-1/50023-0

[28] Schaub, H., and Junkins, J. L., *Analytical Mechanics of Space Systems*, 3rd ed., AIAA, Reston, VA, 2014.
https://doi.org/10.2514/4.102400

[29] Markley, F. L., and Crassidis, J. L., *Sensors and Actuators*, Springer, New York, 2014, pp. 123–181.
https://doi.org/10.1007/978-1-4939-0802-8_4

[30] van Bezooijen, R., Anderson, K., and Ward, D., "Performance of the AST-201 Star Tracker for the Microwave Anisotropy Probe," *Guidance, Navigation and Control Conference*, AIAA Paper 2002-4582, 2002.

[31] Iskenderian, T., “Lessons Learned from Selecting and Testing Spaceflight Potentiometers,” *The 28th Aerospace Mechanisms Symposium*, NASA Lewis Research Center CP-3260, 1994, pp. 339–358.

[32] Anderson, C., “LEWIS Spacecraft Mission Failure Investigation Board,” U.S. Air Force Research Lab. Final Rept., Wright–Patterson AFB, OH, 1998, https://spacese.spacegrant.org/Failure%20Reports/Lewis_MIB_2-98.pdf.

[33] O’Keefe, S. A., and Schaub, H., “Gyro Accuracy and Failure Sensitivity of Underdetermined Coarse Sun Heading Estimation,” *AAS/AIAA Space Flight Mechanics Meeting*, AAS Paper 15-344, Springfield, VA, 2015.

[34] Teil, T., Schaub, H., and Piggott, S., “Comparing Coarse Sun Sensor Based Sequential Sun Heading Filters,” *AAS Guidance and Control Conference*, AAS Paper 18-011, Springfield, VA, 2018.

[35] Crassidis, J. L., and Markley, F. L., “Unscented Filtering for Spacecraft Attitude Estimation,” *Journal of Guidance, Control, and Dynamics*, Vol. 26, No. 4, 2003, pp. 536–542. https://doi.org/10.2514/2.5102

[36] der Merwe, R. V., and Wan, E. A., “The Square-Root Unscented Kalman Filter for State and Parameter-Estimation,” *2001 IEEE International Conference on Acoustics, Speech, and Signal Processing. Proceedings (Cat. No. 01CH37221)*, Vol. 6, IEEE Publ., Piscataway, NJ, 2001, pp. 3461–3464. https://doi.org/10.1109/ICASSP.2001.940586

[37] Shuster, M. D., and Oh, S. D., “Three-Axis Attitude Determination from Vector Observations,” *Journal of Guidance, Control, and Dynamics*, Vol. 4, No. 1, 1981, pp. 70–77. https://doi.org/10.2514/3.19717

[38] Alcorn, J., and Schaub, H., “Simulating Attitude Actuation Options Using the Basilisk Astrodynamics Software Architecture,” *67th International Astronautical Congress*, IAC Paper IAC-16.C1.1.4, Guadalajara, Mexico, 2016.

[39] Kenneally, P. W., Piggott, S., and Schaub, H., “Basilisk: A Flexible, Scalable and Modular Astrodynamics Simulation Framework,” *7th International Conference on Astrodynamics Tools and Techniques (ICATT)*, ICATT, 2018.

[40] Savitzky, A., and Golay, M. J. E., “Smoothing and Differentiation of Data by Simplified Least Squares Procedures,” *Analytical Chemistry*, Vol. 36, No. 8, 1964, pp. 1627–1639. https://doi.org/10.1021/ac60214a047

D. Spencer
Associate Editor